



HAL
open science

Digital Volume Correlation for Large Deformations of Soft Tissues: Pipeline and Proof of Concept for the application to Breast ex vivo Deformations

Thomas Lavigne, Arnaud Mazier, Antoine Perney, Stéphane Pierre Alain Bordas, François Hild, Jakub Lengiewicz

► To cite this version:

Thomas Lavigne, Arnaud Mazier, Antoine Perney, Stéphane Pierre Alain Bordas, François Hild, et al.. Digital Volume Correlation for Large Deformations of Soft Tissues: Pipeline and Proof of Concept for the application to Breast ex vivo Deformations. *Journal of the mechanical behavior of biomedical materials*, 2022, 136, pp.105490. 10.1016/j.jmbbm.2022.105490 . hal-03792835

HAL Id: hal-03792835

<https://hal.science/hal-03792835>

Submitted on 30 Sep 2022

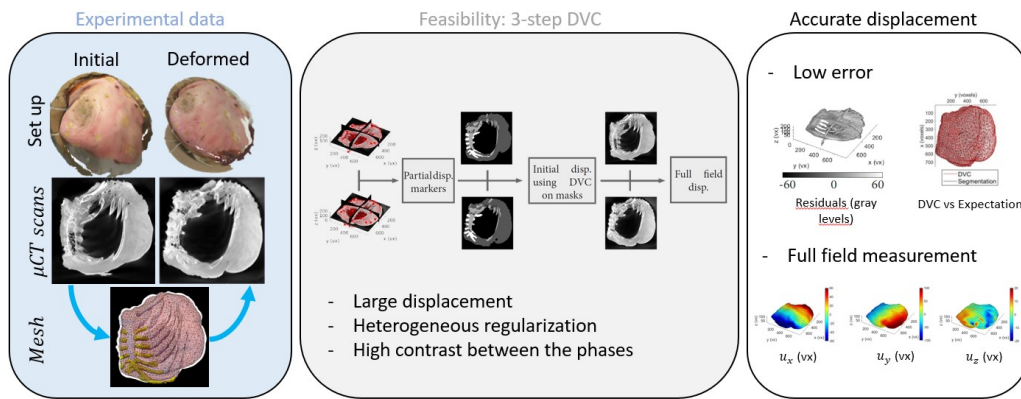
HAL is a multi-disciplinary open access archive for the deposit and dissemination of scientific research documents, whether they are published or not. The documents may come from teaching and research institutions in France or abroad, or from public or private research centers.

L'archive ouverte pluridisciplinaire **HAL**, est destinée au dépôt et à la diffusion de documents scientifiques de niveau recherche, publiés ou non, émanant des établissements d'enseignement et de recherche français ou étrangers, des laboratoires publics ou privés.

Graphical Abstract

Digital Volume Correlation for Large Deformations of Soft Tissues: Pipeline and Proof of Concept for the application to Breast *ex vivo* Deformations

T. Lavigne, A. Mazier, A. Perney, S. P.A. Bordas, F. Hild, J. Lengiewicz



Highlights

Digital Volume Correlation for Large Deformations of Soft Tissues: Pipeline and Proof of Concept for the application to Breast *ex vivo* Deformations

T. Lavigne, A. Mazier, A. Perney, S. P.A. Bordas, F. Hild, J. Lengiewicz

- Three-step DVC pipeline to measure large displacements with only two X-ray scans
- Heterogeneous and regularized DVC was carried out to account for hard/soft tissues
- A large amplitude displacement field was accurately measured for a breast

Digital Volume Correlation for Large Deformations of Soft Tissues: Pipeline and Proof of Concept for the application to Breast *ex vivo* Deformations

T. Lavigne^a, A. Mazier^a, A. Perney^{a,d}, S. P.A. Bordas^{a,e,*}, F. Hild^c,
J. Lengiewicz^{a,b}

^a*Institute of Computational Engineering, Department of Engineering, University of Luxembourg, 6, avenue de la Fonte, Esch-sur-Alzette, L-4364, Luxembourg*

^b*Institute of Fundamental Technological Research, Polish Academy of Sciences (IPPT PAN), Pawinskiego 5B, Warsaw, 02-106, Poland*

^c*University Paris-Saclay, CentraleSupélec, ENS Paris-Saclay, CNRS, LMPS–Laboratoire de Mécanique Paris-Saclay, 4 avenue des Sciences, Gif-sur-Yvette, 91190, France*

^d*Centre des Matériaux, Mines ParisTech, PSL University, 63-65 Rue Henri Auguste Desbrières, Corbeil-Essonnes, 91100, France*

^e*Visiting, Department of Medical Research, China Medical University Hospital, China Medical University, Taichung, Taiwan*

Abstract

Being able to reposition tumors from prone imaging to supine surgery stances is key for bypassing current invasive marking used for conservative breast surgery. This study aims to demonstrate the feasibility of using Digital Volume Correlation (DVC) to measure the deformation of a female quarter thorax between two different body positioning when subjected to gravity. A segmented multipart mesh (bones, cartilage and tissue) was constructed and a three-step FE-based DVC procedure with heterogeneous elastic regularization was implemented. With the proposed framework, the large displacement field of a mixed hard/soft breast sample was recovered with low registration

*Corresponding author

Email address: `stephane.bordas@alum.northwestern.edu` (S. P.A. Bordas)

residuals and low error between the measured and the manually determined deformations of inter-phase interfaces. The present study showed the capacity of FE-based DVC to faithfully capture large deformations of hard/soft tissues.

Keywords: Digital Volume Correlation, Elastic regularization, Hard/soft tissues, Large displacements, Kinematic fields, X-ray tomography

1 **1. Introduction**

2 According to the World Health Organization, “as of the end of 2020,
3 there were 7.8 million women alive who were diagnosed with breast can-
4 cer in the past 5 years, making it the world’s most prevalent cancer.” In
5 breast cancer treatment, surgery is one of the most common practices [1]. In
6 breast-conserving surgery, the imaging procedure (*i.e.*, MRI) is conducted in
7 prone configurations while surgery is performed in supine stance [2, 3, 4, 5].
8 Thus, the surgeon has to mentally predict tumor deformations or use invasive
9 markings such as harpoons or radioactive markers to follow tumor motions.
10 Numerical methods may bypass the marking step, which induces additional
11 uncertainties of the procedure. Biomechanical simulations may predict such
12 complex tumor deformations yet require patient-specific data (*e.g.*, material
13 properties, organ geometry, loading and boundary conditions).

14 Accurately characterizing large and complex deformation fields, as is
15 likely to occur with soft tissues, is challenging and several studies tackled
16 such problem [6, 7, 8]. Few of them presented satisfying results or only vali-
17 dated surface displacement fields [9]. Most of the time, these methods solely
18 rely on the finite element method combined with free-form deformers (*e.g.*, B-

19 spline warping of images) or are lacking clinical validation. In this work, it is
20 proposed to measure 3D displacement fields based on *ex vivo* medical images.
21 Usually, women diagnosed with breast cancer undergo MRI and/or mammog-
22 raphy, which are the starting point of surgical procedures [6, 8, 10]. Digi-
23 tal Image Correlation (DIC), stereocorrelation or Digital Volume Correlation
24 (DVC) use similar inputs and provide experimentally measured displacement
25 fields of surfaces or in the bulk [11, 12]. DVC may allow for the development
26 of patient-specific models to estimate tumor motions due to changes in stance
27 between imaging and intra-operative configurations, and will drastically en-
28 rich the surgeon’s knowledge, thereby helping procedure planning. Previous
29 studies showed the possibility of using DIC and stereovision principles on
30 breasts to measure surface stretches. Khatam et al. [13] manually tracked
31 drawn surgical markers and then assessed surface stretches. Such approaches
32 do not give access to fields in the breast bulk, especially internal strain maps.

33 DVC is an experimental technique that allows for the measurement of
34 displacement fields in three dimensions [14]. It is used to extract strain
35 maps in solid mechanics, but mostly for stiff materials [15, 16] such as
36 bones [14, 17, 18, 19, 20, 21, 22, 23] and often relies on the hypothesis of
37 infinitesimal strains between two successive configurations to ensure conver-
38 gence. DVC is gaining interest in the biomechanical field [24, 25, 26]. Re-
39 cently, DVC was applied to study the spine [27, 28]. Several works used DVC
40 to map strain fields for arteries [29], tendons [30], intervertebral disks [31, 32],
41 tissue interfaces with prosthetics [33] or even the mitral valve [34]. Optical
42 coherence elastography/tomography techniques (*e.g.*, for the identification of
43 elastic properties) based on DVC with 3D infinitesimal strain measurements

44 were performed *ex vivo* on mesoscopic (*i.e.*, millimetric regions of interest)
45 human [35] and chicken [36] breast tissues. As DVC requires high quality
46 images to properly converge, the regions of interest are usually of the order
47 of centimeters (due to technical limitations of setups). A breast subjected to
48 gravity from prone to supine positions undergoes large deformations, which
49 calls for registrations of large regions of interest via DVC. As MRIs are ex-
50 pensive and uncomfortable, one envisions that only two MRI scans would be
51 performed. Therefore, two main challenges arise when dealing with breasts,
52 namely, the strain levels may become high between two consecutive acquisi-
53 tions (*i.e.*, they do not satisfy the small strain hypothesis) and the dimension
54 of the region of interest may be large.

55 The following study is a proof of concept that aims to prove the feasibil-
56 ity of using DVC to measure experimental displacement fields for a breast
57 subjected to its weight when imaged in two different angular configurations
58 wrt. gravity. First, the image acquisition, processing and mesh generation
59 procedures are described. Then, DVC and heterogeneous regularization are
60 recalled. Next, a three-step DVC pipeline is discussed to measure the large
61 amplitude deformations of the studied breast. Last, the results are presented
62 and discussed.

63 **2. Material and Methods**

64 *2.1. Image Acquisition*

65 A left quarter of a thorax (of size $0.27\text{ m} \times 0.26\text{ m} \times 0.06\text{ m}$) was extracted
66 from a female corpse. Fifteen biomarkers were placed on the surface and
67 inside the breast to provide some displacement information (Figure 1(a)).

68 These markers were placed by the medical team and assumed rigidly at-
69 tached to the sample using an adhesive surface. The breast was injected
70 with physiological serum to get closer to an *in vivo* configuration and to
71 mimic its initial mechanical properties.

72 The medical images were acquired at Arnaud de Villeneuve Hospital
73 (Montpellier, France) by Prof. Guillaume Captier and AnatoScope company.
74 The use for research purposes of body donations and removals was in ac-
75 cordance with French law according to the decree of April 27, 2022. The
76 patient-specific geometry was imaged via micro-computed tomography using
77 an RX Solutions scanner with a 0.34 mm resolution. This resolution may be
78 considered as low-quality for tomographies as the X-ray scanner allows for
79 values down to 15 μm . The choice of such resolution was motivated by 3
80 reasons. First, high-resolution acquisitions are usually lengthy (*i.e.*, between
81 3 to 4 h). Second, the cadaver tissues will quickly degrade, thereby prevent-
82 ing from performing a second acquisition. Last, the present CT-scans and
83 clinical MRI images have similar resolutions.

84 Two different configurations were acquired, namely, -45° and -60° in
85 the axial plane with no intermediate states (Figure 1(b,c)). The angles were
86 reached using a inclined wooden support on which the breast was fastened
87 using four plastic straps to be compatible with medical imaging procedures.
88 The assembly was manually moved to go from one configuration to the other.
89 The hardware parameters are reported in Appendix A. As the images were
90 not acquired for DVC purposes, different (Tukey) filtering values were used
91 resulting in variable gray level ranges.

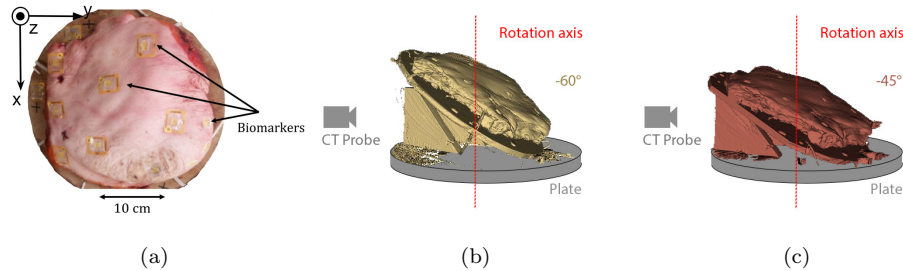


Figure 1: (a) Left quarter of a female thorax ($0.27\text{ m} \times 0.26\text{ m} \times 0.06\text{ m}$ in size) injected with a physiological serum and fastened to a wooden plate using plastic straps. Fifteen biomarkers were placed on the surface and inside the breast. -60° (b) and -45° (c) positions in the CT-scanner for the studied configurations.

92 *2.2. Mesh Generation*

93 Based on the gray levels (Figure 2(a)) and anatomic knowledge, three
 94 entities (phases) were created, namely, breast tissue, bones, and cartilage. A
 95 growth from seeds algorithm was manually initialized (*i.e.*, several slices in
 96 each X, Y, Z direction of the volume were manually “painted” so the algo-
 97 rithm was able to identify regions and gray levels belonging to each individual
 98 phase) within the 3D Slicer software [37]. The result was smoothed, thereby
 99 allowing for mesh generations without too small interface segments as nodes
 100 in different phases had to coincide on interfaces to enforce kinematic compat-
 101 ibility. Last, an artificial outer layer (15 voxels (vx) thick) was added to the
 102 tissue, see Figure 2(b). This “artificial skin” was added to help DVC register
 103 the external surface. Each mask was converted into a sub-mesh and the con-
 104 sidered mesh was the coarsest that was obtained using ScanIP Simpleware
 105 software. With such mesh, sub-voxel elements were avoided.

106 Figure 2(c) shows the resulting volumetric meshes and screenshots of

107 Simpleware software, courtesy of Synopsys. The mesh was composed of
 108 41,454 linear tetrahedra with a characteristic element length of 9.3 ± 2.8 vx
 109 (*i.e.*, 3.2 ± 0.9 mm). To avoid too small elements, 25 of them with length
 110 less than 3 vx were deleted.

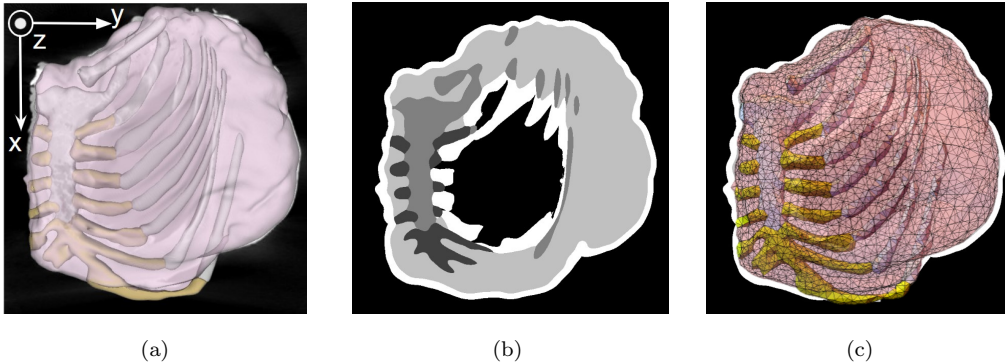


Figure 2: Phase-based mesh construction of the -60° configuration in the axial plane. (a) Phase segmentation (tissue in pink, bones in white and cartilage in yellow) shown on the original scan. (b) Section of a segmented image with the different phases and the artificial skin layer that was added. (c) Phase-based mesh (courtesy of Synopsys) is shown on the original scan.

111 2.3. Regularized Digital Volume Correlation

112 2.3.1. Digital Volume Correlation

113 DVC relies on the conservation of gray levels upon transformations be-
 114 tween two scanned configurations. The cost function Φ_c^2 to be minimized in
 115 global (*e.g.*, FE-based) DVC is generally expressed as [38]

$$\Phi_c^2 = \sum_{ROI} (I_0(\mathbf{x}) - I_t(\mathbf{x} + \mathbf{u}(\mathbf{x})))^2 \quad (1)$$

116 where \mathbf{x} is the position of any voxel in the reference configuration, $\mathbf{u}(\mathbf{x})$
 117 the corresponding continuous displacement vector, and ROI the Region of

118 Interest. The gray levels corresponding to the 3D image of the reference
 119 configuration are denoted by I_0 , and those of the deformed configuration I_t .

120 In the present case, FE-based DVC was considered with 4-noded tetrahe-
 121 dra (*i.e.*, T4 elements [39]). The ROI to be registered during the minimiza-
 122 tion procedure was defined by the considered mesh (Figure 2(c)). Conse-
 123 quently, the unknowns were the nodal displacements gathered in the column
 124 vector $\{\mathbf{v}\}$ such that

$$\mathbf{u}(\mathbf{x}) = \sum_i v_i \mathbf{N}_i^{\text{T4}}(\mathbf{x}) \quad (2)$$

125 where \mathbf{N}_i^{T4} denotes the vectorial shape functions of T4 elements. A modified
 126 Gauss-Newton scheme was used to minimize Φ_c^2 with respect to the sought
 127 nodal displacements $\{\mathbf{v}\}$ [39]

$$\{\mathbf{v}\}^* = \arg \min_{\{\mathbf{v}\}} \Phi_c^2(\{\mathbf{v}\}) \quad (3)$$

128 which leads to iteratively solving linear systems of equations

$$[\mathbf{H}]\{\delta\mathbf{v}\} = \{\mathbf{h}\} \quad (4)$$

129 where $[\mathbf{H}]$ is the DVC Hessian matrix, $\{\mathbf{h}\}$ the residual vector, and $\{\delta\mathbf{v}\}$ the
 130 correction nodal displacement vector.

131 2.3.2. Heterogeneous Regularization

132 As noted in Section 2.1, the images were not originally acquired for DVC
 133 purposes. In particular, the gray level contrast was not optimal. To overcome
 134 this issue, mechanical regularization was considered. It consists in adding a
 135 penalty term to mitigate displacement fluctuations. In regularized DVC,
 136 equilibrium is enforced at the local level by introducing a cost function based

137 on the equilibrium gap (in the absence of body forces) [40]

$$[\mathbf{K}]\{\mathbf{v}\} = \{\mathbf{f}_{\text{res}}\} \quad (5)$$

138 where $[\mathbf{K}]$ is the stiffness matrix, and $\{\mathbf{f}_{\text{res}}\}$ the residual force vector. The
 139 principle of regularization is to supplement the minimized cost function with
 140 the following penalty term

$$\Phi_m^2 = \|\{\mathbf{f}_{\text{res}}\}\|^2 = \{\mathbf{v}\}^\top [\mathbf{K}]^\top [\mathbf{K}]\{\mathbf{v}\} \quad (6)$$

141 One may note that the DVC Hessian matrix $[\mathbf{H}]$ is a 0-th order operator
 142 with respect to displacements (*i.e.*, $[\mathbf{H}]$ depends on the shape functions \mathbf{N}_i^{T4}
 143 themselves, and not on any spatial derivative), and $[\mathbf{K}]$ is a second order
 144 operator [41]; thus $[\mathbf{K}]^\top [\mathbf{K}]$ is a fourth-order operator. To have dimensional
 145 consistency between Φ_c^2 and Φ_m^2 , a regularization length ℓ_{reg} is defined so that
 146 the regularization weight $w_m \propto \ell_{\text{reg}}^4$. The total cost function Φ_{tot}^2

$$\Phi_{\text{tot}}^2 = \Phi_c^2 + w_m \Phi_m^2 \quad (7)$$

147 was minimized iteratively [42]. Convergence was reached when L2-norm of
 148 the displacement corrections becomes less than 10^{-2} vx.

149 In the present study, the ROI covered three different materials (*i.e.*, soft
 150 tissue, cartilage, and bones). To account for the fact that their elastic prop-
 151 erties were very different, heterogeneous regularization was utilized [43]. As a
 152 consequence, each element e was assigned an elastic contrast C^e whose value
 153 was the ratio of the Young's modulus of the phase it belonged to divided by
 154 that of the soft tissue. Thus, $C^e > 1$ corresponds to a phase stiffer than the
 155 soft tissue.

156 The regularization length, ℓ_{reg} , scales with the square root of the elastic
157 contrast C^e [44]. For example, if $C^e = 100$, then the regularization length is
158 ten times higher (*i.e.*, $\sqrt{100}$ factor) for the considered element in comparison
159 to the tissue elements. In all the analyses reported herein, the regularization
160 lengths refer to the softest phase.

161 A convergence study was carried out to determine the best regulariza-
162 tion length. Let us refer to the bone with the index \bullet_b , cartilage with the
163 index \bullet_c , and to tissue with the index \bullet_t . The bone Young's modulus was
164 found to vary between 5 to 50 GPa [45, 46, 47], and that of cartilage in the
165 range from 8 to 40 MPa [48, 49, 50]. Breasts are made of different materi-
166 als such as adipose, fibroglandular, skin, or fascia tissues. In addition to a
167 wide variability between patients, the differences between *in vivo/ex vivo* or
168 compression/tension mechanical tests give a large range of Young's moduli
169 ranging between 0.2 to 28 kPa [51, 52]. Therefore, the elastic contrasts were
170 set to $C_b = 10^6$, $C_c = 10^4$ and $C_t = 1$. Comparisons were also performed to
171 results with two other contrasts, namely, $C_b = 10^3$, $C_c = 10^2$, $C_t = 1$ and
172 $C_b = C_c = C_t = 1$ (*i.e.*, homogeneous properties).

173 2.3.3. DVC Steps to Measure Breast Deformation

174 Regularized DVC was applied to measure breast deformation between
175 -60° axial to -45° axial configurations. The analysis consists of the following
176 three steps.

177 For the first step, an initial evaluation of the mean deformation gradi-
178 ent tensor, \mathbf{F} , was obtained, which was based on the motion of $m = 15$
179 biomarkers. The biomarkers were manually identified while segmenting the
180 scans. For each configuration, their position was measured as the geomet-

181 ric barycenter of their segmentation. Therefore, one may consider that the
 182 resulting positions include some user uncertainty resulting from the segmen-
 183 tation procedure. This first step corresponds to current practices in which
 184 markers are put on the external surface of the breast, and their motions are
 185 sought for tumor repositioning.

186 Let \mathbf{x}_m denote the position of the m -th marker in the reference configu-
 187 ration, and $\mathbf{x}_m + \mathbf{u}_m$ its position in the deformed configuration. Considering
 188 the deformation gradient tensor \mathbf{F} , the translation vector \mathbf{t} , and the second
 189 order identity tensor \mathbf{I} , the approximated field \mathbf{u}_a reads

$$\mathbf{u}_a(\mathbf{x}_m, \mathbf{F}, \mathbf{t}) = (\mathbf{F} - \mathbf{I})\mathbf{x}_m + \mathbf{t} \quad (8)$$

190 where the components of \mathbf{F} and \mathbf{t} were obtained by least squares minimization

$$[\mathbf{F}^*, \mathbf{t}^*] = \arg \min_{\mathbf{F}, \mathbf{t}} \|\mathbf{u}_m - \mathbf{u}_a(\mathbf{x}_m, \mathbf{F}, \mathbf{t})\|^2 \quad (9)$$

191 For the second step, a better approximation of the initial displacement
 192 field was computed with homogeneous regularized DVC applied to the seg-
 193 mented images created for each configuration (Figure 3) including internal
 194 air. Because the histograms of the raw images were not fully conserved, using
 195 such images allowed the gray levels to be made identical for each segmented
 196 phase. This DVC step was initialized by the marker-based displacement esti-
 197 mate. No elastic contrast was considered to allow for the correct positioning
 198 of the bones. Given the fact that the three phases had uniform gray levels,
 199 the gray level contrast (*i.e.*, gradient of image) was nonzero only for a very
 200 limited number of voxels (*i.e.*, at interfaces between phases). This property
 201 leads to very steep cost functions about the optimal solution. Blurring the
 202 volume smoothens the cost function and induces faster convergence of the

203 Newton-based minimization scheme. Thus to improve convergence, the two
204 volumes were blurred (with a Gaussian filter with a radius of 3 vx).

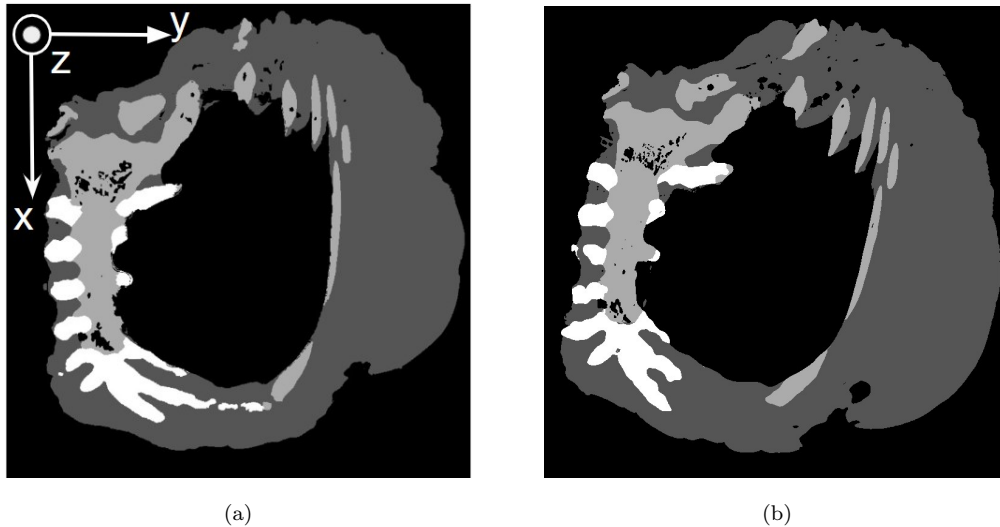


Figure 3: Sections of segmented volumes corresponding to (a) -60° and (b) -45° configurations. Phase-based images were created for the second step (*i.e.*, cartilage in white, bones in light gray, tissue in dark gray and air in black). The phase of confined air was included.

205 For the third step, the previously measured displacement field was used
206 to initialize the heterogeneous regularized DVC calculation on the original
207 volumes (Figure 4), with no filtering of the gray levels. The elastic contrasts
208 were set to the values given in Section 2.3.2. The regularization length was
209 set according to the convergence study (Appendix B).

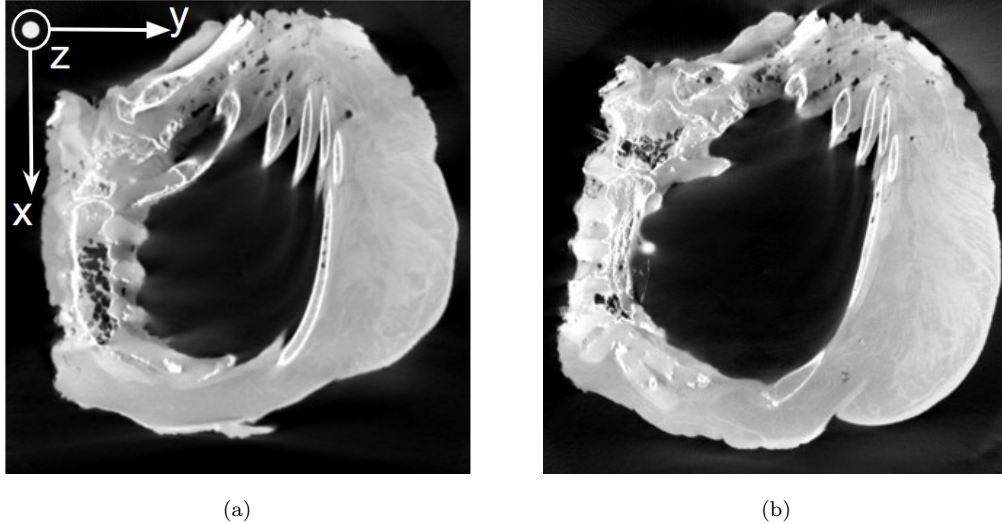


Figure 4: Sections of -60° (a) and -45° (b) configurations obtained with an RX-Solutions CT-scanner (voxel size of 0.34 mm) in the axial plane. These volumes were used during the third step of the DVC procedure.

210 While the gray level residuals $\rho(\mathbf{x}) = I_0(\mathbf{x}) - I_t(\mathbf{x} + \mathbf{u}(\mathbf{x}))$ of DVC analyses
 211 provide a quality indicator for the measured displacement field (see Equa-
 212 tion (1)), the Root Mean Square Error (RMSE) was used as a metric for
 213 evaluating the trustworthiness of surface displacements.

$$\text{RMSE}^2 = \frac{1}{N} \sum_{i=1}^N (\mathbf{x}_i^{\text{DVC}} - \mathcal{P}^{\text{seg}}(\mathbf{x}_i^{\text{DVC}}))^2 \quad (10)$$

214 For each phase of both initial and deformed configurations, a surface (STL)
 215 mesh was generated from the volumetric mesh by identifying the boundary
 216 elements. Then, the measured displacement field was applied to the initial
 217 surface nodes. For each phase, the error between the assessed N deformed
 218 nodes from DVC \mathbf{x}^{DVC} and the refined mesh resulting from the segmentation
 219 of the deformed image \mathcal{M}^{seg} was computed as the root mean square error

220 (RMSE). As the meshes did not have the same number of nodes, a projection
221 operator \mathcal{P}^{seg} of the DVC deformed nodes onto \mathcal{M}^{seg} was assessed using an
222 Iterative Closest Point (ICP) algorithm [53].

223 2.3.4. Uncertainty quantification

224 As pointed out above, the imaging conditions were not optimal for DVC
225 purposes and thus may degrade the measurement uncertainties. Further-
226 more, common practice requires at least two repeat scans to be acquired to
227 quantify kinematic uncertainties *a priori* [38, 54]. In the present case, no
228 repeat scan was performed. Thus another (*a posteriori*) route was followed.
229 At the end of any global DVC analysis, the quality of registration is probed
230 by analyzing the gray level residuals ρ , which contain information about ac-
231 quisition noise and artifacts, as well as indications about the trustworthiness
232 of the selected kinematic bases [55, 38]. It was thus decided to artificially
233 create a new volume by applying a 0.5 vx translation along all three Carte-
234 sian coordinates to the reference volume. White Gaussian noise was also
235 added (Figure 5(b)), whose standard deviation σ_ρ was that of the gray level
236 residuals corresponding to the result of the DVC analysis that was deemed
237 the most trustworthy in the sequel. This volume was correlated with the
238 reference volume (Figure 5(a)). The displacement uncertainties correspond
239 to the standard deviations of nodal displacements in each direction. Sim-
240 ilarly, the strain uncertainties were assessed as the standard deviations of
241 elementary strains. As regularized DVC was carried out, the fine mesh was
242 not altered but the regularization length ℓ_{reg} was varied to assess standard
243 uncertainties [56, 57].

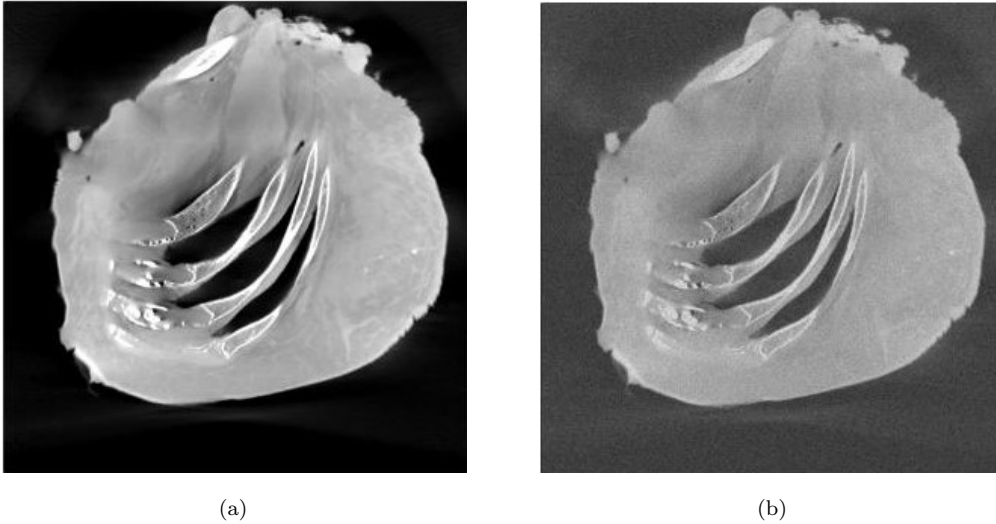


Figure 5: Sections of -60° original volume (a) and translated volume (b) corrupted with white Gaussian noise whose standard deviation was equal to 18.3 gray levels

244 3. Results and Discussion

245 3.1. DVC Results

246 In the following results, the mean element size was equal to 10 voxels,
247 and the mean spatial resolution was 17 voxels (the physical voxel size was
248 0.34 mm).

249 The marker-based displacement field was computed and applied to the
250 mesh as an initial guess (Figure 6), which provided a good approximation
251 to recover the overall shape of the sample in the deformed configuration.
252 Because the biomarkers were mainly placed on the surface, the initial guess
253 suffered from inaccuracy in the volume (*e.g.*, near bones) and led to high
254 RMS residual (63 gray levels).

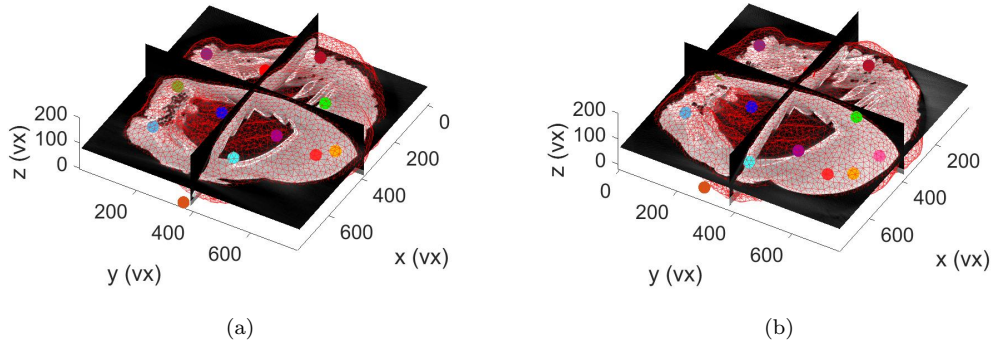


Figure 6: (a) Reference (-60°) and (b) deformed (-45°) meshes based on the marker motions. The wireframe meshes are superimposed over orthoslices of their respective volumes. The biomarkers are shown as colored disks.

255 This first estimate served as initialization for the DVC analysis between
 256 the segmented images (for which the gray level distribution was almost the
 257 same (Figure 7(b))). Therefore, gray level conservation was enforced. The
 258 regularization length was set to 35 vx to properly converge (*i.e.*, only 48 DVC
 259 iterations were needed). The use of these segmented images allowed for fur-
 260 ther reducing the gray level residuals (Figure 7(b)). The final RMS residual
 261 was 10.6 gray levels (Figure 7), which is deemed low given the complexity of
 262 the deformation and the acquisition conditions. It is worth noting that the
 263 initial RMS level was equal to 62.7 gray levels, which proves that the current
 264 practice (*i.e.*, first step) is not sufficient for a precise determination of the
 265 tumor position.

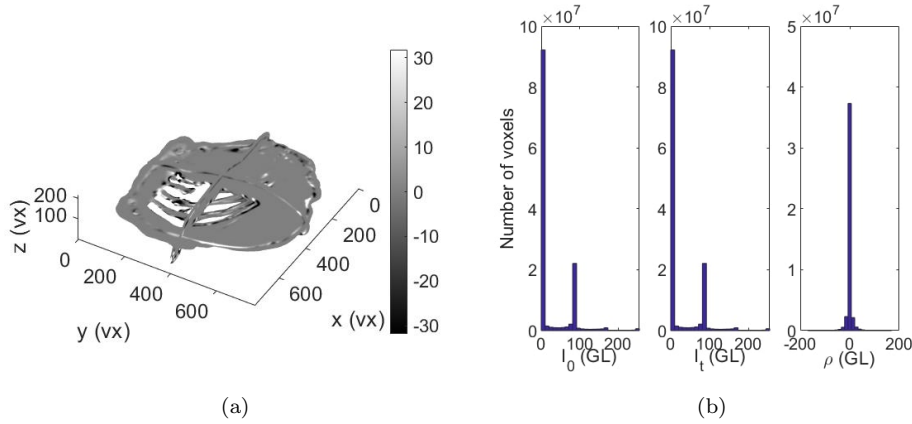


Figure 7: (a) Gray level residuals are shown within the region of interest defined by the considered mesh. (b) From left to right: gray level histograms of the reference volume I_0 , deformed volume I_t , and DVC residuals ρ shown in sub-figure (a).

266 Figure 8 shows the measured displacement field. The tissue phase shifted
 267 downward, thereby creating an inframammary fold (Figure 11(d)). Thanks
 268 to the segmented images, this complex configuration could be recovered.
 269 Adding the artificial skin layer was a key step to ensure tracking of the
 270 interface between the tissue and air. Without such gray level contrast, the
 271 procedure could have converged to the wrong positions. However, this result
 272 is only the first approximation as no gray level contrast existed inside each
 273 phase (Figure 3). It is worth noting that the displacement amplitudes were
 274 very high in all three directions. Without good initialization, such levels are
 275 not accessible with only two volumes to register. The biomarkers on the
 276 one hand, and the artificial skin on the other hand were key to getting such
 277 results.

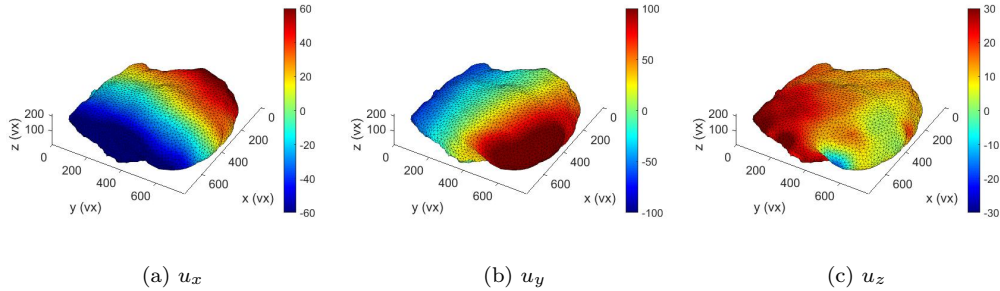


Figure 8: Displacement field expressed in voxels ($1 \text{ vx} \equiv 0.34 \text{ mm}$) for the DVC analysis on the segmented images. (a) u_x , (b) u_y and (c) u_z components plotted on the deformed mesh.

278 In the final step, DVC was run with the actual 3D images when initialized
 279 with the displacement field shown in Figure 8 applying a contrast of $C_b =$
 280 10^6 , $C_c = 10^4$, $C_t = 1$. To probe the effect of regularization, the analysis
 281 was started with a large regularization length (*i.e.*, $\ell_{\text{reg}} = 40 \text{ vx}$). Once
 282 convergence was achieved, a new analysis was run with a lower regularization
 283 length (*i.e.*, $\ell_{\text{reg}} = 20 \text{ vx}$), and so on down to 0.5 vx . The upper bound was
 284 selected as higher values led to bad conditioning of the DVC Hessian matrix,
 285 especially when heterogeneous elastic contrasts were considered.

286 Figure 9(a) shows the change of the RMS gray level residual as a function
 287 of the regularization length. There is a very significant decrease in RMS
 288 residual with ℓ_{reg} , thereby indicating that results with large regularization
 289 lengths should not be kept. This trend can be understood from the fact
 290 that body forces were not negligible for the tissue. In the present case, the
 291 penalty term follows the hypothesis of vanishing body forces. This is not
 292 valid as the soft tissue deformed due to gravity contrary to the other phases,
 293 which are stiffer and do not deform. Therefore the penalty term should be as

294 small as possible and very small regularization should be applied. Since the
 295 elastic contrasts were very high for the bone and cartilage, the regularization
 296 in the tissue was essentially vanishing for the lower regularization lengths.
 297 This trend was observed for the three considered contrasts. However, when
 298 $C_b = 10^6$, $C_c = 10^4$, $C_t = 1$, the residual significantly increase before the
 299 other two cases. This difference is due to the large value of regularization
 300 length of bone and cartilage, which degrades the conditioning of the Hessian
 301 matrices.

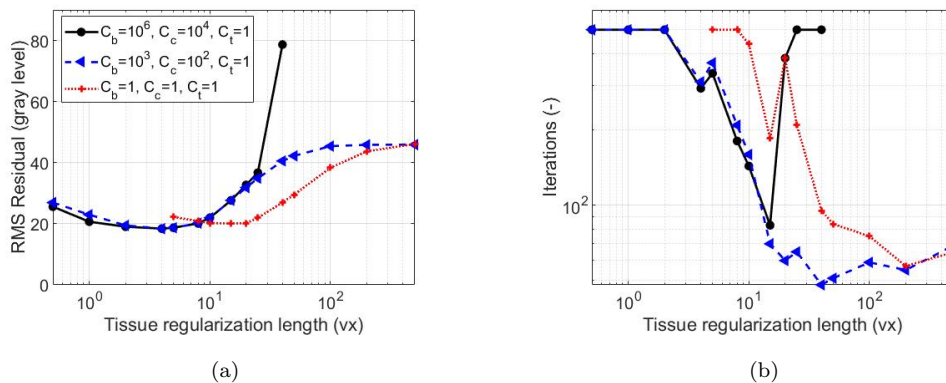


Figure 9: Convergence analysis. (a) RMS gray level residuals and (b) number of iterations of the DVC algorithm as functions of the regularization length ℓ_{reg} for three different elastic contrast settings

302 To analyze convergence of the DVC algorithm, the number of iterations
 303 to reach convergence is displayed in Figure 9(b). As the regularization length
 304 was decreased, the number of iterations augmented for all the applied con-
 305 trast triplets. This trend was expected as less and less weight (*i.e.*, smaller
 306 ℓ_{reg}) was put on the tissue phase. Given the complexity of the sought
 307 deformation and the fact that the gray level contrast was not very high,

308 such trend was unavoidable. For regularization lengths less than 3 vx when
 309 $C_b = 10^6$, $C_c = 10^4$, $C_t = 1$ (or 3 vx when $C_b = 10^3$, $C_c = 10^2$, $C_t = 1$
 310 and 8 vx when $C_b = C_c = C_t = 1$), the number of iterations became very
 311 high (*i.e.*, convergence in terms of L2-norm of the displacement corrections
 312 less than 10^{-2} vx was no longer satisfied before the maximum number of
 313 iterations was reached).

314 It is worth noting that to properly capture the inframammary fold (Fig-
 315 ure 11(d)), a significant number of iterations was needed when $\ell_{\text{reg}} = 4$ vx
 316 (Figure 9(b)), which led to a solution with one of the lowest RMS residuals
 317 (Figure 9(a)) for the highest considered elastic contrast. Further conver-
 318 gence studies are shown in Appendix B. By introducing elastic contrast, it
 319 was also possible to lower the regularization length in the tissue (*i.e.*, 4 vx for
 320 $C_b = 10^6$, $C_c = 10^4$, $C_t = 1$ instead of 20 vx for $C_b = 1$, $C_c = 1$, $C_t = 1$) to
 321 reach a lower final residual (18.3 instead of 20.2 gray level for homogeneous
 322 regularization). Introducing elastic contrast allowed for strongly penalizing
 323 the hard phase and limiting the regularization over the soft phase which was
 324 therefore freer to move. All three convergence curves (Figure 9(a)) have
 325 the same trend but higher contrasts allowed for significantly relaxing the
 326 constraints on the soft tissue.

327 From these two different quantities, the results obtained for a regular-
 328 ization length of 4 vx with heterogeneous regularization ($C_b = 10^6$, $C_c =$
 329 10^4 , $C_t = 1$) were kept. 292 iterations were required to converge. The RMS
 330 residuals were equal to 18.3 gray levels (Figure 10(a)). They were almost two
 331 times higher than those observed for the segmented volumes. However, given
 332 the fact that no special care was taken in the acquisition process, such levels

333 are more than acceptable. Figure 10(b) shows an almost centered distribu-
 334 tion of the residuals with minimal bias, even though gray level conservation
 335 was not fully satisfied because of the followed acquisition protocol. As the
 336 scans were not acquired for DVC purposes, no effort was put into keeping the
 337 same filter values, which resulted in slightly different gray level distributions.

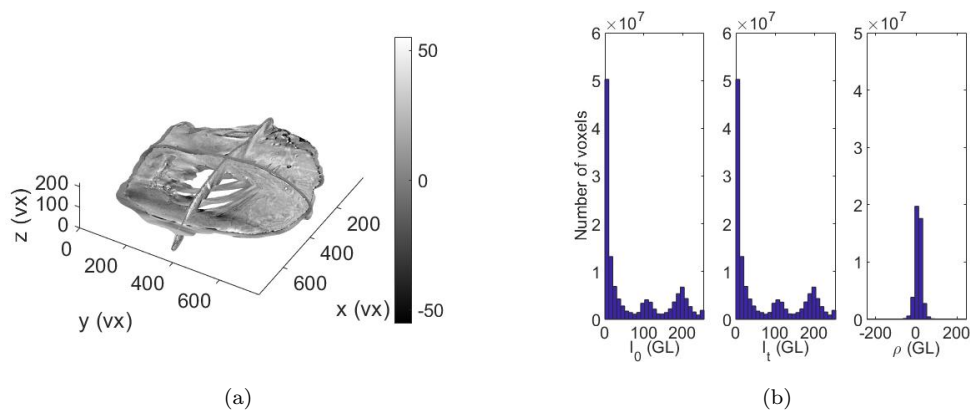


Figure 10: (a) Gray level residuals for the last DVC analysis. (b) From left to right: gray level histograms of the reference volume I_0 , deformed volume I_t , and DVC residuals ρ shown in sub-figure (a).

338 Figure 11 shows the measured displacement field. Similarly to the re-
 339 sults achieved with the segmented volumes, the tissue moved downward and
 340 created an inframammary fold (Figure 11(d)). In all three directions, the
 341 displacement amplitudes were high (*i.e.*, of the order of centimeters). The
 342 mask-based initialization allowed the DVC analysis to be started from a good
 343 initial guess, and the presence of gray level contrast in the phases gave more
 344 accurate and local information on the displacement field (as an example, see
 345 u_z component in Figures 8(c) and 11(c)).

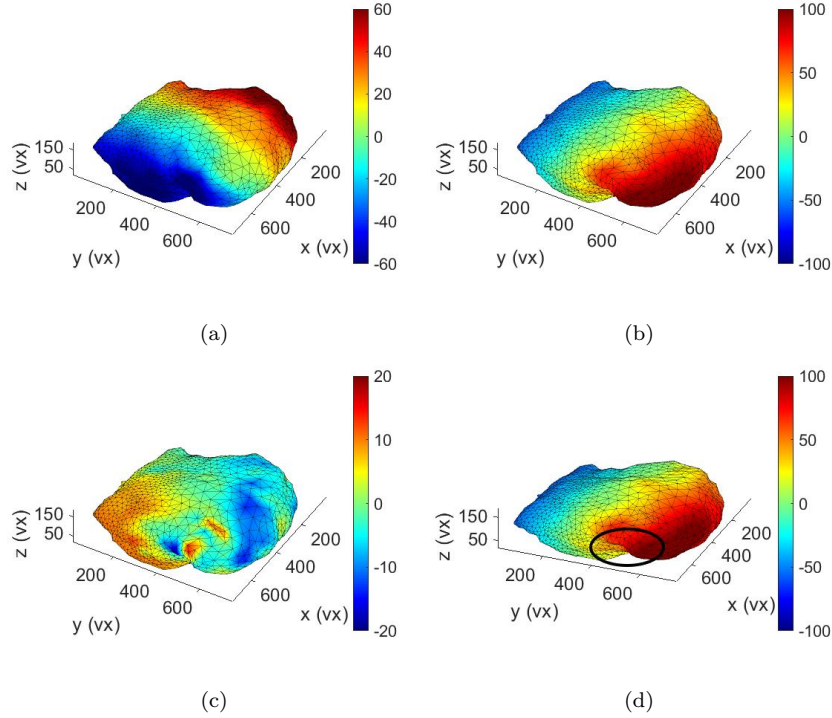


Figure 11: Displacement fields expressed in voxels ($1 \text{ vx} \equiv 0.34 \text{ mm}$) for the last DVC analysis displayed on the mesh without the outer skin layer. (a) u_x , (b) u_y and (c) u_z components plotted on the deformed mesh. (d) u_y component from another viewpoint to highlight the displacement discontinuity around the inframammary fold (black ellipse).

346 The soft tissue experienced very large displacements, part of them due to
 347 rigid body motions (*i.e.*, translations and rotations), but also to mechanical
 348 strains. In the present case, the Green-Lagrange strains ($\mathbf{E} = \frac{1}{2} (\mathbf{F}^\top \mathbf{F} - \mathbf{I})$)
 349 are reported. They were estimated from the exact differentiation of the
 350 shape functions of the 4-noded tetrahedra (*i.e.*, T4 elements) to evaluate
 351 the deformation gradient tensor \mathbf{F} . Figure 12 shows that the soft tissue
 352 underwent large strains (including shear in particular in the inframammary
 353 fold) up to 25% in magnitude, which is large between two scans only.

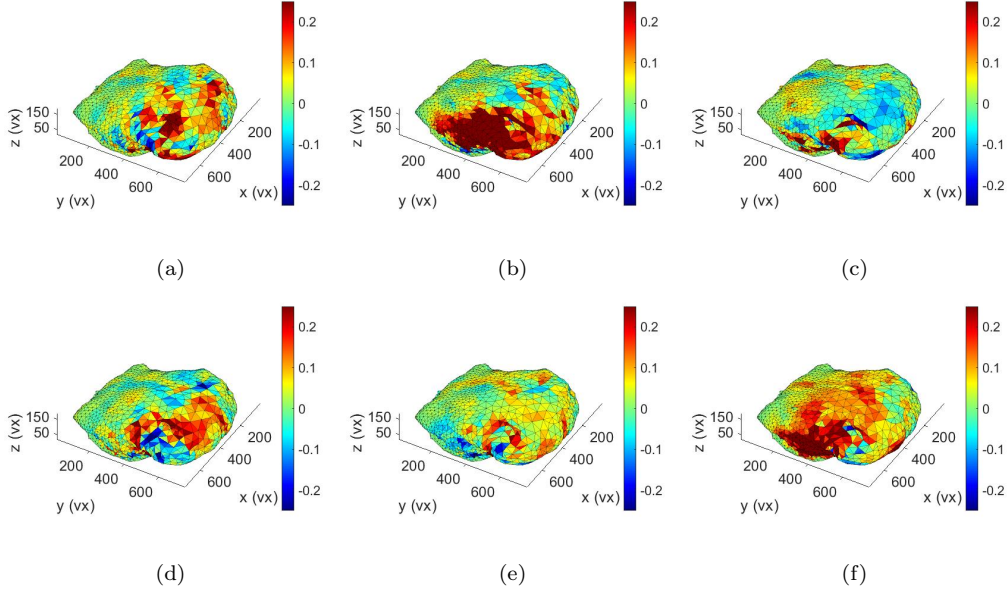


Figure 12: Strain fields for the last DVC analysis displayed on the mesh without the skin layer. (a) E_{xx} , (b) E_{yy} , (c) E_{zz} , (d) E_{xy} , (e) E_{xz} and (f) E_{yz} components. The soft tissue underwent large strains (including shear in particular in the inframammary fold) up to 25% in magnitude.

354 3.2. *A posteriori* uncertainty quantification

355 The DVC results obtained for a regularization length of 4 vx with $C_b =$
 356 10^6 , $C_c = 10^4$, $C_t = 1$ led to residuals whose standard deviation was equal
 357 to 18.3 gray levels. With this information, the standard uncertainties σ were
 358 assessed *a posteriori* by varying the regularization length ℓ_{reg} . Figure 13(a)
 359 shows that the larger the regularization length, the lower the standard dis-
 360 placement uncertainty. This dependence illustrates the trade-off between
 361 measurement uncertainty and spatial resolution (here corresponding the reg-
 362 ularization length) [58, 57]. The power law interpolation with exponent -1.5
 363 describes very well the reported results in accordance with the hypothesis

364 of white Gaussian noise [56, 58]. Similarly, the standard strain uncertainties
 365 also follow very closely a power law with exponent -2.5 (Figure 13(b)).

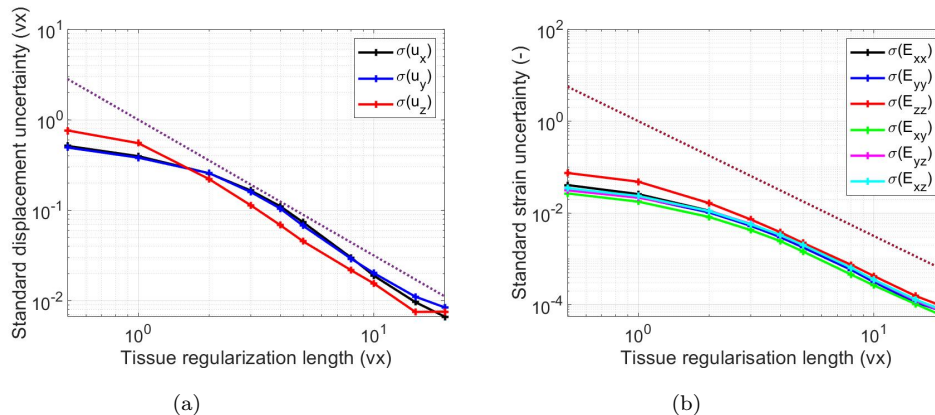


Figure 13: Standard displacement (a) and strain (b) uncertainties as functions of the regularization length ℓ_{reg} for an elastic contrast of $C_b = 10^6$, $C_c = 10^4$ and $C_t = 1$. The dashed lines show power law interpolations with exponent -1.5 for the displacements and -2.5 for the strains.

366 With the selected regularization length ($\ell_{\text{reg}} = 4 \text{ vx}$) and elastic contrasts
 367 ($C_b = 10^6$, $C_c = 10^4$, $C_t = 1$), the standard displacement uncertainties were
 368 of the order of 0.1 vx, and the corresponding standard strain uncertainties
 369 were less than 5×10^{-3} . These levels are deemed sufficiently low in comparison
 370 to the reported results (Figures 11 and 12).

371 3.3. Further validation

372 Last, the overall shape of the sample was well recovered (Figure 14). In
 373 addition to the gray level residuals, in Table 1 the RMSE (Equation 10) was
 374 used as a metric for evaluating the trustworthiness of surface displacements.
 375 The measured error was a few millimeters (between 2.2 to 3.1 mm, which

376 corresponds to a range of 6.8 to 9.4 vx). When the highest elastic contrasts
 377 were considered, all errors decreased about 0.1 mm in comparison to homo-
 378 geneous regularization, which further validates their use. As the error was
 379 lower than the mean element size (*i.e.*, 10 vx) and the mean spatial resolu-
 380 tion (*i.e.*, 17 vx), the measured displacement field was very realistic. It is
 381 worth remembering that this error included those due to the segmentation
 382 steps. As this multiphase sample had a complex morphology, and internal
 383 gray level contrast, the segmentation relied on coupling of growing from seeds
 384 algorithms, and smoothing with operator-dependent steps. The latter ones
 385 explain parts of the observed mismatches.

Table 1: RMSE computed between the DVC deformed surface and the corresponding segmented surface. The data in parentheses correspond to homogeneous regularization and the other ones to the highest elastic contrasts

Phase	RMSE (mm)
Soft tissue	2.2 (2.3)
Cartilage	3.1 (3.2)
Bones	2.6 (2.7)

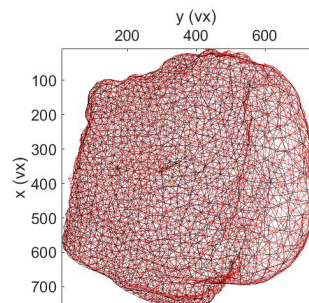


Figure 14: Superposition of the deformed mesh resulting from DVC (red) with the expected mesh obtained from the segmentation of the deformed configuration (black).

386 4. Conclusion

387 The objective of this work was to demonstrate the feasibility of using
 388 DVC to measure large biomechanical deformations. More specifically, the

389 displacement field was measured for a breast subjected to gravity in two
390 different positions when imaged via computed tomography. To obtain satis-
391 factory results, a three-step DVC pipeline was implemented. The first step
392 consisted in determining the motions of 15 biomarkers, which corresponds to
393 one of the current clinical practices. It was shown that these motions were
394 not sufficient to properly map the whole deformation field of the breast. The
395 second step used the previous initial guess to assess the breast deformation
396 with segmented volumes in which the three phases (*i.e.*, bone, cartilage and
397 soft tissue) were distinguished. An external skin was added to allow for the
398 inframammary fold to be better captured. With these new motions, a final
399 set of DVC analyses was performed on the original reconstructed volumes
400 accounting for elastic contrasts in the three phases.

401 The results of this proof of concept study highlighted the efficiency of
402 the DVC technique for a breast including the inframammary fold. Elastic
403 contrasts were set according to literature data. The studied breast had re-
404 gions with very high elastic contrast (10^6 between bones and tissue, and 10^4
405 for cartilage), which was accounted for in the regularized DVC scheme used
406 herein. Few DVC iterations were needed to quickly pre-converge to a suitable
407 displacement field with a low RMS residual. The convergence study wrt. the
408 regularization length showed that a rather low value could be chosen to ob-
409 tain accurate results. If the regularization length was too large, meaningful
410 displacement fluctuations were filtered out. Conversely, when the regulariza-
411 tion length was too small, then convergence issues arose. Similar trends were
412 observed for two other sets of elastic contrasts presented, thereby showing
413 that the higher the contrast, the lower the regularization length (*i.e.*, having

414 a higher contrast, less regularization was applied to the soft tissue leading to
415 lower registration residuals).

416 The present study had several limitations. First, the tomographic acquisi-
417 tions were not optimal for DVC purposes. In particular, no repeat scans were
418 performed for uncertainty quantifications. As only two scans were available,
419 an *a posteriori* route was followed to assess standard kinematic uncertain-
420 ties. Furthermore, CT-scans (but MRIs) are generally not used in clinical
421 applications. Therefore, further studies are needed to investigate the fea-
422 sibility of the present DVC pipeline when applied to MRIs. Second, the
423 experiment was carried out on an *ex vivo* injected cadaverous breast to be
424 close to *in vivo* testing conditions. Therefore, this study may be extended
425 to living tissues. It is hypothesized that blood flow between various acqui-
426 sitions may impact the resulting gray levels and thus DVC results. This
427 study also had user-dependent steps to be followed. The segmentation was
428 manually assessed and the biomarker positions were assessed from their seg-
429 mentation. For the patient geometry, some uncertainties and mismatches
430 were observed between the gray level images and the associated segment
431 (*i.e.*, the mesh needed sufficiently regular elements and simplifications of the
432 geometry, namely, smoothing and simplification of the regions were neces-
433 sary). Future studies are needed to automate these steps to reduce likely
434 user-impact on the results.

435 Last, the results obtained herein may then be used in a calibration pipeline
436 to get patient-specific material parameters. As the displacement field was
437 computed for a finite element (FE) discretization, links with finite element
438 simulations are straightforward. One would be able to predict the deforma-

439 tion of the organ in surgical positions. The DVC analysis may also be coupled
440 with finite element analyses in cases of (self-)contact. The computed FE dis-
441 placement field may then serve as initialization for DVC registrations. Its
442 trustworthiness would then be probed thanks to the gray level residuals.

443 **5. Declaration of competing interest**

444 The authors have no conflicts of interest to report.

445 **6. Acknowledgment**

446 This study was supported by the European Union’s Horizon 2020 re-
447 search and innovation program under grant agreement No 811099, the Marie
448 Skodowska-Curie, Luxembourg grant agreement No. 764644, and the FNR
449 Project No. C20/MS/14782078/QuaC. JL would like to acknowledge the
450 support from EU Horizon 2020 Marie Skodowska Curie Individual Fellow-
451 ship MOrPhEM under Grant 800150. The medical images used in the
452 present study were obtained at Hopital Arnaud de Villeneuve, Département
453 de Gynécologie Obstétrique in collaboration with Dr. Gauthier Rathat, Prof.
454 Guillaume Captier, and AnatoScope. The authors would like to thank Syn-
455 opsys for its support in providing access to the Simpleware software to gener-
456 ate the meshes used in this project, and RX-Solutions for their support and
457 answers about the machine settings that were used. Last, the authors sin-
458 cerely thank the person who donated her body to science so that anatomical
459 research could be performed.

460 **Appendix A. DVC hardware parameters**

Orientation	-60°	-45°
Tomograph	EasyTom 150 (RX Solution)	EasyTom 150 (RX Solution)
Target / Anode	W (reflection mode)	W (reflection mode)
Voltage	120 kV	120 kV
Current	202 μ A	202 μ A
Focal spot size	50 μ m	50 μ m
Tube to detector	610 mm	610 mm
Tube to object	430 mm	430 mm
Detector	Varian 25 \times 20 cm	Varian 25 \times 20 cm
Definition	1920 \times 1536 pixels	1920 \times 1536 pixels
Projection definition	1840 \times 728 pixels	1840 \times 728 pixels
Number of projections	2111	1407
Angular amplitude	360°	360°
Frame average	15 per projection	15 per projection
Frame rate	30 fps	30 fps
Acquisition duration	28 min 08 sec	18 min 40 sec
Reconstruction algorithm	filtered back-projection	filtered back-projection
Filter	Tukey (75%)	Tukey (0%)
Gray Levels amplitude	8 bits	8 bits
Volume size	768 \times 781 \times 216 voxels (after crop)	768 \times 781 \times 216 voxels (after crop)
Field of view	261.12 \times 265.54 \times 73.44 mm ³ (after crop)	261.12 \times 265.54 \times 73.44 mm ³ (after crop)
Image scale	0.34 mm/voxel	0.34 mm/voxel

461 Appendix B. Convergence Analysis

462 The deformed meshes obtained in the convergence analysis for homo-
463 geneous regularization (*i.e.*, $C_b = C_c = C_t = 1$, see red dotted curve of
464 Figure 9(a)), are displayed in Figure B.15 when the regularization length
465 was relaxed from an initially very high value ($\ell_{\text{reg}} = 500 \text{ vx}$) to a very small
466 one ($\ell_{\text{reg}} = 5 \text{ vx}$). In the last case, virtually no regularization was applied
467 to the soft tissue. As shown in Figure 9(a), the RMS residuals decreased
468 with the regularization length. Figure 9(b) shows that a high regulariza-
469 tion may help to converge quickly but tends to an unsatisfactory solution for
470 which the lower fold cannot be captured. When the regularization length was
471 lowered, the fold was better recovered until a minimum length was reached
472 (*i.e.*, about 10 vx in the present case, see Figure B.15(e)). For low regulariza-
473 tion lengths, the minimization procedure no longer converged (Figure 9(b))
474 to a trustworthy solution. It is worth remembering that the main cause of
475 the soft tissue to deform was due to gravity. Since mechanical regularization
476 was based on minimizing the equilibrium gap, its weight should not be too
477 high to avoid nonphysical solutions. The results shown hereafter illustrate
478 this phenomenon.

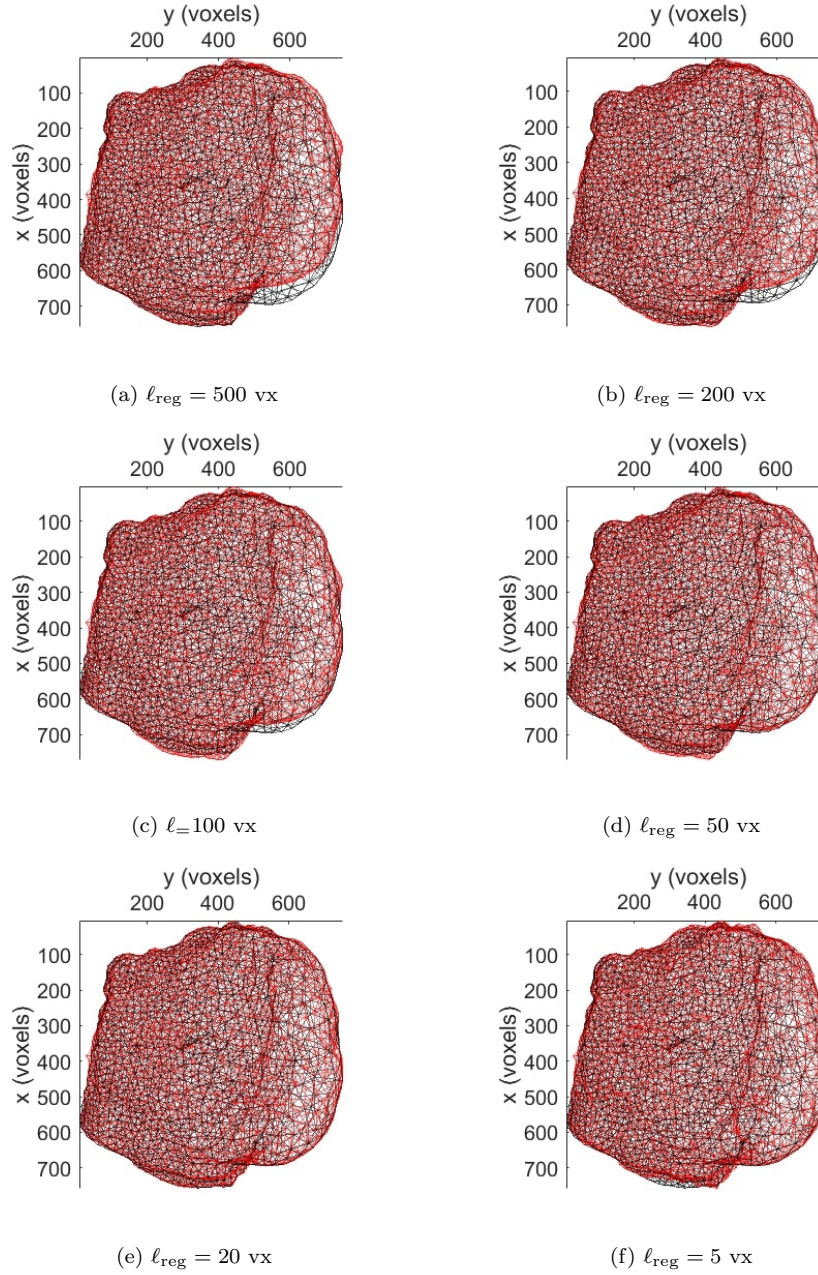


Figure B.15: Evolution of the deformed mesh with the regularization length. Segmentation results are in a black wireframe and the DVC results are in red. (a) $\ell_{\text{reg}} = 500 \text{ vx}$, (b) $\ell_{\text{reg}} = 200 \text{ vx}$, (c) $\ell_{\text{reg}} = 100 \text{ vx}$, (d) $\ell_{\text{reg}} = 50 \text{ vx}$, (e) $\ell_{\text{reg}} = 20 \text{ vx}$ and (f) $\ell_{\text{reg}} = 5 \text{ vx}$.

479 **References**

480 [1] C. E. DeSantis, J. Ma, M. M. Gaudet, L. A. Newman, K. D.
481 Miller, A. G. Sauer, A. Jemal, R. L. Siegel, Breast cancer statistics,
482 2019, CA: A Cancer Journal for Clinicians 69 (2019) 438–451. URL:
483 <https://doi.org/10.3322/caac.21583>. doi:10.3322/caac.21583.

484 [2] J. Georgii, T. Paetz, M. Harz, C. Stoecker, M. Rothgang, J. Colletta,
485 K. Schilling, M. Schlooz-Vries, R. M. Mann, H. K. Hahn, Simulation
486 and visualization to support breast surgery planning, in: A. Tingberg,
487 K. Lång, P. Timberg (Eds.), Breast Imaging, Springer International
488 Publishing, Cham, 2016, pp. 257–264.

489 [3] V. Rajagopal, Modelling Breast Tissue Mechanics Under Gravity Load-
490 ing, PhD thesis, University of Auckland (New-Zealand), 2007. URL:
491 http://www.esc.auckland.ac.nz/nash/publications/rajagopal_boundthesis_may2007...

492 [4] V. Rajagopal, P. Nielsen, M. Nash, Modeling breast biomechanics
493 for multi-modal image analysis-successes and challenges, Wiley inter-
494 disciplinary reviews. Systems biology and medicine 2 (2010) 293–304.
495 doi:10.1002/wsbm.58.

496 [5] A. Mazier, S. Ribes, B. Gilles, S. P. Bordas, A rigged model of the breast
497 for preoperative surgical planning, Journal of Biomechanics 128 (2021)
498 110645. URL: <https://doi.org/10.1016/j.jbiomech.2021.110645>.
499 doi:10.1016/j.jbiomech.2021.110645.

500 [6] A. W. C. Lee, J. A. Schnabel, V. Rajagopal, P. M. F. Nielsen, M. P.
501 Nash, Breast image registration by combining finite elements and free-

- 502 form deformations, in: J. Martí, A. Oliver, J. Freixenet, R. Martí (Eds.),
503 Digital Mammography, Springer Berlin Heidelberg, Berlin, Heidelberg,
504 2010, pp. 736–743.
- 505 [7] V. Rajagopal, M. P. Nash, R. P. Highnam, P. M. F. Nielsen, The
506 breast biomechanics reference state for multi-modal image analysis, in:
507 E. A. Krupinski (Ed.), Digital Mammography, Springer Berlin Heidel-
508 berg, Berlin, Heidelberg, 2008, pp. 385–392.
- 509 [8] D. J. Gavaghan, J. P. Whiteley, S. J. Chapman, J. M. Brady, P. Path-
510 manathan, Predicting tumor location by modeling the deformation of
511 the breast, IEEE Transactions on Biomedical Engineering 55 (2008)
512 2471–2480. doi:10.1109/TBME.2008.925714.
- 513 [9] B. Eiben, V. Vavourakis, J. H. Hipwell, S. Kabus, C. Lorenz,
514 T. Buelow, N. R. Williams, M. Keshtgar, D. J. Hawkes, Surface
515 driven biomechanical breast image registration, in: R. J. W. III,
516 Z. R. Yaniv (Eds.), Medical Imaging 2016: Image-Guided Procedures,
517 Robotic Interventions, and Modeling, volume 9786, International So-
518 ciety for Optics and Photonics, SPIE, 2016, pp. 282 – 291. URL:
519 <https://doi.org/10.1117/12.2216728>. doi:10.1117/12.2216728.
- 520 [10] M. Duraes, P. Crochet, E. Pagès, E. Grauby, L. Lasch, L. Rebel, F. Van
521 Meer, G. Rathat, Surgery of nonpalpable breast cancer: First step to
522 a virtual per-operative localization? First step to virtual breast cancer
523 localization, Breast Journal 25 (2019) 874–879. doi:10.1111/tbj.13379.
- 524 [11] M. Sutton, J. Orteu, H. Schreier, Image correlation for shape, motion

- 525 and deformation measurements: Basic Concepts, Theory and Applica-
526 tions, Springer, New York, NY (USA), 2009.
- 527 [12] M. Sutton, Computer vision-based, noncontacting deformation mea-
528 surements in mechanics: A generational transformation, *Appl. Mech.*
529 *Rev.* 65 (2013) 050802.
- 530 [13] H. Khatam, G. P. Reece, M. C. Fingeret, M. K. Markey,
531 K. Ravi-Chandar, In-vivo quantification of human breast de-
532 formation associated with the position change from supine to
533 upright, *Medical Engineering & Physics* 37 (2015) 13–22.
534 URL: <https://doi.org/10.1016/j.medengphy.2014.09.016>.
535 doi:10.1016/j.medengphy.2014.09.016.
- 536 [14] B. Bay, T. Smith, D. Fyhrie, M. Saad, Digital volume correlation:
537 three-dimensional strain mapping using X-ray tomography, *Exp. Mech.*
538 39 (1999) 217–226.
- 539 [15] B. Bay, Methods and applications of digital volume correlation, *J. Strain*
540 *Analysis* 43 (2008) 745–760.
- 541 [16] A. Buljac, C. Jailin, A. Mendoza, J. Neggers, T. Taillandier-Thomas,
542 A. Bouterf, B. Smaniotto, F. Hild, S. Roux, Digital volume correlation:
543 Review of progress and challenges, *Experimental Mechanics* 58 (2018)
544 661–708. URL: <https://doi.org/10.1007/s11340-018-0390-7>.
545 doi:10.1007/s11340-018-0390-7.
- 546 [17] L. Liu, E. F. Morgan, Accuracy and precision of digi-
547 tal volume correlation in quantifying displacements and strains

- 548 in trabecular bone, *Journal of Biomechanics* 40 (2007) 3516–
549 3520. URL: <https://doi.org/10.1016/j.jbiomech.2007.04.019>.
550 doi:10.1016/j.jbiomech.2007.04.019.
- 551 [18] A. Benoit, S. Guérard, B. Gillet, G. Guillot, F. Hild, D. Mitton, J.-N.
552 Périé, S. Roux, 3D analysis from micro-MRI during in situ compression
553 on cancellous bone, *Journal of Biomechanics* 42 (2009) 2381–2386.
- 554 [19] A. I. Hussein, P. E. Barbone, E. F. Morgan, Digital volume correlation
555 for study of the mechanics of whole bones, *Procedia IUTAM* 4 (2012)
556 116–125. URL: <https://doi.org/10.1016/j.piutam.2012.05.013>.
557 doi:10.1016/j.piutam.2012.05.013.
- 558 [20] F. Gillard, R. Boardman, M. Mavrogordato, D. Hollis, I. Sin-
559 clair, F. Pierron, M. Browne, The application of digital vol-
560 ume correlation (dvc) to study the microstructural behaviour of
561 trabecular bone during compression, *Journal of the Mechan-
562 ical Behavior of Biomedical Materials* 29 (2014) 480–499. URL:
563 <https://www.sciencedirect.com/science/article/pii/S1751616113003159>.
564 doi:<https://doi.org/10.1016/j.jmbbm.2013.09.014>.
- 565 [21] M. Peña Fernández, S. J. Sasso, S. McPhee, C. Black, J. Kanc-
566 zler, G. Tozzi, U. Wolfram, Nonlinear micro finite element models
567 based on digital volume correlation measurements predict early
568 microdamage in newly formed bone, *Journal of the Mechan-
569 ical Behavior of Biomedical Materials* 132 (2022) 105303. URL:
570 <https://www.sciencedirect.com/science/article/pii/S1751616122002168>.
571 doi:<https://doi.org/10.1016/j.jmbbm.2022.105303>.

- 572 [22] M. Palanca, S. Oliviero, E. Dall'Ara, Microfe models of porcine
573 vertebrae with induced bone focal lesions: Validation of predicted
574 displacements with digital volume correlation, *Journal of the Me-*
575 *chanical Behavior of Biomedical Materials* 125 (2022) 104872. URL:
576 <https://www.sciencedirect.com/science/article/pii/S1751616121005087>.
577 doi:<https://doi.org/10.1016/j.jmbbm.2021.104872>.
- 578 [23] D. Wu, T. Joffre, C. Öhman Mägi, S. J. Ferguson, C. Persson,
579 P. Isaksson, A combined experimental and numerical method to
580 estimate the elastic modulus of single trabeculae, *Journal of the*
581 *Mechanical Behavior of Biomedical Materials* 125 (2022) 104879. URL:
582 <https://www.sciencedirect.com/science/article/pii/S1751616121005130>.
583 doi:<https://doi.org/10.1016/j.jmbbm.2021.104879>.
- 584 [24] M. Palanca, G. Tozzi, L. Cristofolini, The use of dig-
585 ital image correlation in the biomechanical area: a
586 review, *International Biomechanics* 3 (2015) 1–21.
587 URL: <https://doi.org/10.1080/23335432.2015.1117395>.
588 doi:10.1080/23335432.2015.1117395.
- 589 [25] C. M. Disney, P. D. Lee, J. A. Hoyland, M. J. Sherratt, B. K. Bay, A
590 review of techniques for visualising soft tissue microstructure deforma-
591 tion and quantifying strain ex vivo, *JOURNAL OF MICROSCOPY*
592 272 (2018) 165–179. doi:10.1111/jmi.12701, 5th Annual Symposium on
593 Tomography for Scientific Advancement (ToScA), Univ Portsmouth,
594 Portsmouth, ENGLAND, 2017.
- 595 [26] E. Dall'Ara, A. Bodey, H. Isaksson, G. Tozzi, A practical

- 596 guide for in situ mechanical testing of musculoskeletal tis-
597 sues using synchrotron tomography, *Journal of the Mechani-*
598 *cal Behavior of Biomedical Materials* 133 (2022) 105297. URL:
599 <https://www.sciencedirect.com/science/article/pii/S1751616122002107>.
600 doi:<https://doi.org/10.1016/j.jmbbm.2022.105297>.
- 601 [27] G. Tozzi, E. Dall’Ara, M. Palanca, M. Curto, F. Innocente, L. Cristo-
602 folini, Strain uncertainties from two digital volume correlation
603 approaches in prophylactically augmented vertebrae: Local analysis
604 on bone and cement-bone microstructures, *Journal of the Me-*
605 *chanical Behavior of Biomedical Materials* 67 (2017) 117–126. URL:
606 <https://www.sciencedirect.com/science/article/pii/S1751616116304222>.
607 doi:<https://doi.org/10.1016/j.jmbbm.2016.12.006>.
- 608 [28] M. Ruspi, M. Palanca, C. Faldini, L. Cristofolini, Full-field in vitro
609 investigation of hard and soft tissue strain in the spine by means of
610 digital image correlation, *Muscles, Ligaments and Tendons Journal*
611 07 (2019) 538. URL: <https://doi.org/10.32098/mltj.04.2017.08>.
612 doi:[10.32098/mltj.04.2017.08](https://doi.org/10.32098/mltj.04.2017.08).
- 613 [29] V. A. A. Santamaria, M. F. Garcia, J. Molimard, S. Avril, Character-
614 ization of chemoelastic effects in arteries using digital volume correla-
615 tion and optical coherence tomography, *ACTA BIOMATERIALIA* 102
616 (2020) 127–137. doi:[10.1016/j.actbio.2019.11.049](https://doi.org/10.1016/j.actbio.2019.11.049).
- 617 [30] J. Sartori, S. Kohring, S. Bruns, J. Moosmann, J. U. Hammel,
618 Gaining insight into the deformation of achilles tendon entheses

- 619 in mice, *ADVANCED ENGINEERING MATERIALS* 23 (2021).
620 doi:10.1002/adem.202100085.
- 621 [31] C. M. Disney, J. Mo, A. Eckersley, A. J. Bodey, J. A. Hoyland,
622 M. J. Sherratt, A. A. Pitsillides, P. D. Lee, B. K. Bay, Regional
623 variations in discrete collagen fibre mechanics within intact interver-
624 tebral disc resolved using synchrotron computed tomography and digi-
625 tal volume correlation, *ACTA BIOMATERIALIA* 138 (2022) 361–374.
626 doi:10.1016/j.actbio.2021.10.012.
- 627 [32] C. M. Disney, A. Eckersley, J. C. McConnell, H. Geng, A. J. Bodey,
628 J. A. Hoyland, P. D. Lee, M. J. Sherratt, B. K. Bay, Synchrotron to-
629 mography of intervertebral disc deformation quantified by digital volume
630 correlation reveals microstructural influence on strain patterns, *ACTA*
631 *BIOMATERIALIA* 92 (2019) 290–304. doi:10.1016/j.actbio.2019.05.021.
- 632 [33] K. Rankin, J. Steer, J. Paton, M. Mavrogordato, A. Marter, P. Wors-
633 ley, M. Browne, A. Dickinson, Developing an analogue residual limb for
634 comparative dvc analysis of transtibial prosthetic socket designs, *MA-*
635 *TERIALS* 13 (2020). doi:10.3390/ma13183955.
- 636 [34] E. L. Pierce, C. H. Bloodworth, A. Naran, T. F. Easley, M. O.
637 Jensen, A. P. Yoganathan, Novel method to track soft tissue deforma-
638 tion by micro-computed tomography: Application to the mitral valve,
639 *ANNALS OF BIOMEDICAL ENGINEERING* 44 (2016) 2273–2281.
640 doi:10.1007/s10439-015-1499-9.
- 641 [35] A. Nahas, M. Bauer, S. Roux, A. C. Boccara, 3d static elastography

- 642 at the micrometer scale using full field OCT, *Biomedical Optics Ex-*
643 *press* 4 (2013) 2138. URL: <https://doi.org/10.1364/boe.4.002138>.
644 doi:10.1364/boe.4.002138.
- 645 [36] F. Meng, C. Chen, S. Hui, J. Wang, Y. Feng, C. Sun, Three-
646 dimensional static optical coherence elastography based on
647 inverse compositional gauss-newton digital volume correla-
648 tion, *Journal of Biophotonics* 12 (2019) e201800422. URL:
649 <https://onlinelibrary.wiley.com/doi/abs/10.1002/jbio.201800422>.
650 doi:<https://doi.org/10.1002/jbio.201800422>.
651 arXiv:<https://onlinelibrary.wiley.com/doi/pdf/10.1002/jbio.201800422>.
- 652 [37] A. Fedorov, R. Beichel, J. Kalpathy-Cramer, J. Finet, J.-C.
653 Fillion-Robin, S. Pujol, C. Bauer, D. Jennings, F. Fennessy,
654 M. Sonka, J. Buatti, S. Aylward, J. V. Miller, S. Pieper, R. Kiki-
655 nis, 3d slicer as an image computing platform for the quanti-
656 tative imaging network, *Magnetic Resonance Imaging* 30 (2012)
657 1323–1341. URL: <https://doi.org/10.1016/j.mri.2012.05.001>.
658 doi:10.1016/j.mri.2012.05.001.
- 659 [38] A. Buljac, C. Jailin, A. Mendoza, T. Taillandier-Thomas, A. Bouterf,
660 J. Neggers, B. Smaniotto, F. Hild, S. Roux, Digital volume correla-
661 tion: Review on progress and challenges, *Exp. Mech.* (2018). URL:
662 <http://doi.org/10.1007/s11340-018-0390-7>.
- 663 [39] F. Hild, A. Bouterf, L. Chamoin, F. Mathieu, J. Neggers, F. Pled,
664 Z. Tomičević, S. Roux, Toward 4d mechanical correlation, *Adv. Mech.*
665 *Simul. Eng. Sci.* 3 (2016) 1–26.

- 666 [40] D. Claire, F. Hild, S. Roux, A finite element formulation to identify
667 damage fields: The equilibrium gap method, *Int. J. Num. Meth. Engng.*
668 61 (2004) 189–208.
- 669 [41] A. Mendoza, J. Neggens, F. Hild, S. Roux, Complete Mechanical Regu-
670 larization Applied to Digital Image and Volume Correlation, *Computer*
671 *Methods in Applied Mechanics and Engineering* 355 (2019) 27–43.
- 672 [42] F. Hild, S. Roux, Digital image correlation, in: P. Rastogi, E. Hack
673 (Eds.), *Optical Methods for Solid Mechanics. A Full-Field Approach*,
674 Wiley-VCH, Weinheim (Germany), 2012, pp. 183–228.
- 675 [43] A. Tsitova, F. Bernachy-Barbe, B. Bary, S. A. Dandachli, C. Bourcier,
676 B. Smaniotto, F. Hild, Damage quantification via digital volume
677 correlation with heterogeneous mechanical regularization: Application
678 to an in situ meso-flexural test on mortar, *Experimental Mechan-*
679 *ics* (2021). URL: <https://doi.org/10.1007/s11340-021-00778-7>.
680 doi:10.1007/s11340-021-00778-7.
- 681 [44] R. Naylor, F. Hild, C. Fagianio, M. Hirsekorn, Y. Renollet, B. Tranquart,
682 E. Baranger, Mechanically regularized FE DIC for heterogeneous ma-
683 terials, *Experimental Mechanics* 59 (2019) 1159–1170.
- 684 [45] J. Y. Rho, R. B. Ashman, C. H. Turner, Young's mod-
685 ulus of trabecular and cortical bone material: Ultrasonic and
686 microtensile measurements, *Journal of Biomechanics* 26 (1993)
687 111–119. URL: [https://doi.org/10.1016/0021-9290\(93\)90042-d](https://doi.org/10.1016/0021-9290(93)90042-d).
688 doi:10.1016/0021-9290(93)90042-d.

- 689 [46] K. D. Hunt, V. D. O'Loughlin, D. W. Fitting, L. Adler, Ultrasonic
690 determination of the elastic modulus of human cortical bone, *Med-
691 ical & Biological Engineering & Computing* 36 (1998) 51–56. URL:
692 <https://doi.org/10.1007/bf02522857>. doi:10.1007/bf02522857.
- 693 [47] B. B. Seedhom, E. Berry, A. E. Ostell, M. Cuppone, The
694 longitudinal young's modulus of cortical bone in the mid-
695 shaft of human femur and its correlation with CT scanning
696 data, *Calcified Tissue International* 74 (2004) 302–309. URL:
697 <https://doi.org/10.1007/s00223-002-2123-1>. doi:10.1007/s00223-
698 002-2123-1.
- 699 [48] J. L. Forman, R. W. Kent, Modeling costal cartilage us-
700 ing local material properties with consideration for gross het-
701 erogeneities, *Journal of Biomechanics* 44 (2011) 910–916.
702 URL: <https://doi.org/10.1016/j.jbiomech.2010.11.034>.
703 doi:10.1016/j.jbiomech.2010.11.034.
- 704 [49] L. W. Huwe, W. E. Brown, J. C. Hu, K. A. Athanasiou, Char-
705 acterization of costal cartilage and its suitability as a cell source
706 for articular cartilage tissue engineering, *Journal of Tissue En-
707 gineering and Regenerative Medicine* 12 (2018) 1163–1176. URL:
708 <https://doi.org/10.1002/term.2630>. doi:10.1002/term.2630.
- 709 [50] M. Griffin, G. O'Toole, W. Sabbagh, M. Szarko, P. Butler, Comparison
710 of the compressive mechanical properties of auricular and costal carti-
711 lage from patients with microtia, *Journal of Biomechanics* 103 (2020)

- 712 109688. URL: <https://doi.org/10.1016/j.jbiomech.2020.109688>.
713 doi:10.1016/j.jbiomech.2020.109688.
- 714 [51] Y. Payan, J. Ohayon, Biomechanics of Living Organs: Hy-
715 perelastic Constitutive Laws for Finite Element Modeling,
716 Biomechanics of Living Organs, Elsevier Science, 2017. URL:
717 <https://books.google.fr/books?id=9WVJvgAACAAJ>.
- 718 [52] A. Míra, A.-K. Carton, S. Muller, Y. Payan, A biomechanical
719 breast model evaluated with respect to mri data collected in three
720 different positions, *Clinical Biomechanics* 60 (2018) 191–199. URL:
721 <https://www.sciencedirect.com/science/article/pii/S0268003318301426>.
722 doi:<https://doi.org/10.1016/j.clinbiomech.2018.10.020>.
- 723 [53] P. J. Besl, N. D. McKay, A Method for Registration of 3-D Shapes,
724 *IEEE Transactions on Pattern Analysis and Machine Intelligence* 14
725 (1992) 239–256. doi:10.1109/34.121791.
- 726 [54] A. Buljac, T. Taillandier-Thomas, L. Helfen, T. Morgeneyer, F. Hild,
727 Evaluation of measurement uncertainties of digital volume correlation
728 applied to laminography data, *Journal of Strain Analysis for Engineering*
729 *Design* 53 (2018) 49–65.
- 730 [55] F. Hild, A. Bouterf, S. Roux, Damage Measurements via DIC, *Interna-*
731 *tional Journal of Fracture* 191 (2015) 77–105.
- 732 [56] H. Leclerc, J. Périé, S. Roux, F. Hild, Voxel-scale digital volume corre-
733 lation, *Exp. Mech.* 51 (2011) 479–490.

- 734 [57] T. Taillandier-Thomas, S. Roux, T. Morgeneyer, F. Hild, Localized
735 strain field measurement on laminography data with mechanical regu-
736 larization, *Nucl. Inst. Meth. Phys. Res. B* 324 (2014) 70–79.
- 737 [58] H. Leclerc, J. Périé, F. Hild, S. Roux, Digital volume correlation: What
738 are the limits to the spatial resolution?, *Mech. & Indust.* 13 (2012)
739 361–371.

740 **List of Figures**

741 1 (a) Left quarter of a female thorax ($0.27\text{ m} \times 0.26\text{ m} \times 0.06\text{ m}$
742 in size) injected with a physiological serum and fastened to
743 a wooden plate using plastic straps. Fifteen biomarkers were
744 placed on the surface and inside the breast. -60° (b) and -45°
745 (c) positions in the CT-scanner for the studied configurations. 6

746 2 Phase-based mesh construction of the -60° configuration in
747 the axial plane. (a) Phase segmentation (tissue in pink, bones
748 in white and cartilage in yellow) shown on the original scan.
749 (b) Section of a segmented image with the different phases and
750 the artificial skin layer that was added. (c) Phase-based mesh
751 (courtesy of Synopsys) is shown on the original scan. 7

752 3 Sections of segmented volumes corresponding to (a) -60° and
753 (b) -45° configurations. Phase-based images were created for
754 the second step (*i.e.*, cartilage in white, bones in light gray,
755 tissue in dark gray and air in black). The phase of confined
756 air was included. 12

757 4 Sections of -60° (a) and -45° (b) configurations obtained with
758 an RX-Solutions CT-scanner (voxel size of 0.34 mm) in the
759 axial plane. These volumes were used during the third step of
760 the DVC procedure. 13

761 5 Sections of -60° original volume (a) and translated volume (b)
762 corrupted with white Gaussian noise whose standard deviation
763 was equal to 18.3 gray levels 15

764	6	(a) Reference (-60°) and (b) deformed (-45°) meshes based on	
765		the marker motions. The wireframe meshes are superimposed	
766		over orthoslices of their respective volumes. The biomarkers	
767		are shown as colored disks.	16
768	7	(a) Gray level residuals are shown within the region of interest	
769		defined by the considered mesh. (b) From left to right: gray	
770		level histograms of the reference volume I_0 , deformed volume	
771		I_t , and DVC residuals ρ shown in sub-figure (a).	17
772	8	Displacement field expressed in voxels ($1 \text{ vx} \equiv 0.34 \text{ mm}$) for	
773		the DVC analysis on the segmented images. (a) u_x , (b) u_y and	
774		(c) u_z components plotted on the deformed mesh.	18
775	9	Convergence analysis. (a) RMS gray level residuals and (b)	
776		number of iterations of the DVC algorithm as functions of the	
777		regularization length ℓ_{reg} for three different elastic contrast	
778		settings	19
779	10	(a) Gray level residuals for the last DVC analysis. (b) From	
780		left to right: gray level histograms of the reference volume	
781		I_0 , deformed volume I_t , and DVC residuals ρ shown in sub-	
782		figure (a).	21
783	11	Displacement fields expressed in voxels ($1 \text{ vx} \equiv 0.34 \text{ mm}$) for	
784		the last DVC analysis displayed on the mesh without the outer	
785		skin layer. (a) u_x , (b) u_y and (c) u_z components plotted on	
786		the deformed mesh. (d) u_y component from another view-	
787		point to highlight the displacement discontinuity around the	
788		inframammary fold (black ellipse).	22

789	12	Strain fields for the last DVC analysis displayed on the mesh	
790		without the skin layer. (a) E_{xx} , (b) E_{yy} , (c) E_{zz} , (d) E_{xy} ,	
791		(e) E_{xz} and (f) E_{yz} components. The soft tissue underwent	
792		large strains (including shear in particular in the inframam-	
793		mary fold) up to 25% in magnitude.	23
794	13	Standard displacement (a) and strain (b) uncertainties as func-	
795		tions of the regularization length ℓ_{reg} for an elastic contrast of	
796		$C_b = 10^6$, $C_c = 10^4$ and $C_t = 1$. The dashed lines show power	
797		law interpolations with exponent -1.5 for the displacements	
798		and -2.5 for the strains.	24
799	14	Superposition of the deformed mesh resulting from DVC (red)	
800		with the expected mesh obtained from the segmentation of the	
801		deformed configuration (black).	25
802	B.15	Evolution of the deformed mesh with the regularization length.	
803		Segmentation results are in a black wireframe and the DVC	
804		results are in red. (a) $\ell_{\text{reg}} = 500$ vx, (b) $\ell_{\text{reg}} = 200$ vx,	
805		(c) $\ell_{\text{reg}} = 100$ vx, (d) $\ell_{\text{reg}} = 50$ vx, (e) $\ell_{\text{reg}} = 20$ vx and	
806		(f) $\ell_{\text{reg}} = 5$ vx.	31

807 **List of Tables**

808 1 RMSE computed between the DVC deformed surface and the
809 corresponding segmented surface. The data in parentheses
810 correspond to homogeneous regularization and the other ones
811 to the highest elastic contrasts 25